Colossal band gap response of single-layer phosphorene to strain predicted by quantum Monte Carlo

Y. Huang,[1] A. Faizan,[2] M. Manzoor,[2] J. Brndiar,[1] L. Mitas ,[3] J. Fabian,[4] and I. Štich [1,2,5,*]

[1]*Institute of Informatics, Slovak Academy of Sciences, 845 07 Bratislava, Slovakia*
[2]*Institute of Physics, Slovak Academy of Sciences, 84511 Bratislava, Slovakia*
[3]*Department of Physics, North Carolina State University, Raleigh, North Carolina 27695-8202, USA*
[4]*University Regensburg, Institute for Theoretical Physics, 93040 Regensburg, Germany*
[5]*Department of Natural Sciences, University of Ss. Cyril and Methodius, 917 01 Trnava, Slovakia*

Straintronics is an emerging field enabling novel tuneable functionalities of electronic, optical, magnetic, or spin devices with advances being fuelled by new developments in van der Walls (vdW) heterostructure engineering and materials design. Here we show, using state-of-the-art quantum Monte Carlo (QMC) methods, that a single phosphorene monolayer exhibits outstanding straintronics functionalities due to discovered colossal strain tunability of its semiconducting electronic gap. First, we determine the equilibrium atomic structure that differs appreciably from available bulk phosphorene experimental data. That enables us to precisely analyze the quasiparticle band gaps for any uniaxial (armchair and zigzag) and biaxial strains which we describe by a quadrivariate paraboloid function of lattice and internal structure parameters. Using the fixed-node QMC calculations fitted by analytical formulas we localize the following excited state crossings: (i) between the direct $(\Gamma \to \Gamma)$ and direct but reordered $(\Gamma \to \Gamma')$ excitations that also imply substantial differences of corresponding transport properties; and (ii) between the direct $\Gamma \to \Gamma$ and indirect $\Gamma \to X$ excitations. Based on this highly accurate many-body treatment, we predict the gauge factor ≈ 100 meV/% and an unusual behavior with the band gap remaining direct even if strained by several percent. Consequently, we suggest there is a colossal band gap tunability window, larger by an order of magnitude when compared to quintessential straintronic materials such as MoS_2. In addition, we ascertain that the ground state deformation energies exhibit an out-of plane negative Poisson's ratio and auxetic behavior.

I. INTODUCTION

Two-dimensional (2D) materials have already revolutionized science and provide ample opportunities for technological breakthroughs due to their unique electronic, optical, thermal, spin, and magnetic properties [1–7]. Electronic structure of a variety of 2D systems exhibit a wide range of electronic states and phases, from metallic to wide band gap insulators, with perhaps the most technologically interesting being 2D semiconductors [8,9]. In particular, materials featuring band gaps in the intermediate range of ≈ 0.3–2 eV are the most promising for prospective device applications. Due to reduced dimensionality and screening, presence of a sizable band gap is often accompanied also by the sought after high carrier mobility. In this respect, some of the most prominent examples of such materials are the transition metal dichalcogenides (TMD) [9] and phosphorene [8].

Once prepared by exfoliation or epitaxy, 2D materials in their natural form may lack the desired properties, such as technologically relevant band gaps. Among many options for further processing, one of the most obvious is layer engineering. For instance, the band gap can be modulated from ≈ 2 eV in a single layer phosphorene (SLP) [8,10], to intermediate values in few-layer black phosphorus (FLP) exfoliated from the bulk black phosphorus (BP) [1,2,11], to 0.3 eV in BP [8]. This range is remarkably large, exhibiting almost an order of magnitude in the band-gap reduction. Less dramatic but still very significant gap change is observed in MoS_2 from 2.15 eV (single-layer) to 1.29 eV in $2H\text{-}MoS_2$ [9]. Interestingly, the band gap is direct at Γ in SLP, FLP, and still direct at Z in BP, whereas it is direct only in the single-layer MoS_2.

2D materials are typically supported by a substrate (quartz, sapphire, etc.) and, as in case of phosphorene, also by capping, which provides dielectric embedding. This offers another possibility for band-gap engineering, for instance, single-layer MoS_2 band gap can be modulated from 2.8 eV to 1.9 eV by dielectric environment [12]. Similar experimental range was reported also for single-layer phosphorene [10].

The other widely used tuning tool, which we explore here, is application of strain [13,14] which can tune such properties continuously. 2D materials are very strainable. For instance, MoS_2 could experimentally be elastically deformed up to 11%

without breaking the material [15] and monolayer phosphorene in a modeling study was found to sustain tensile strain up to 27% and 30% in the zigzag and armchair directions, respectively [16], offering an outstanding potential for use in flexible electronics and for tuning via applied strain. Many straintronic experiments have been performed on 2D MoS_2. For example, tensile strains of up to $\approx 0.5\%$ have been applied with gauge factors of the order of 100 meV/%, i.e., with band gap tuning of few dozens of meV [17]. In contrast, using the highly accurate quantum Monte Carlo methods (QMC) [10,18,19], we predict that single-layer phosphorene not only exhibits a similar band-gap gauge factor to MoS_2 of ≈ 100 meV/%, but, at the same time, it keeps the direct $\Gamma \to \Gamma$ nature of band gap over a very large window of applied compressive/tensile strains, making the tuning of band gap accessible within $\approx \pm 0.5$ eV.

Our use of the benchmark-quality quantum Monte Carlo methods is motivated by our previous result for free-standing SLP in equilibrium [10]. The major mainstream methods, such as Density Functional Theory (DFT) or Many-body perturbation theory within GW approximation (GW), depending on the approximations used, exhibited spreads of the quasiparticle band gaps of the order of ≈ 1 eV. Benchmarking of these various results against experimental results is complicated by experimental uncertainties due to impacts from dielectric embedding, capping, presence of defects, and different sensitivity of experimental probes to their presence, leading to a comparable spread of the experimental values of ≈ 1 eV. Such uncertainty is fairly typical for electronic properties of 2D materials. Therefore, a high quality many-body calculation is highly desirable for understanding the various factors affecting the results and for opening up a path of educated tuning [10].

One can assume that both theoretical and experimental biases will only increase if the material is subjected to strain. Indeed, several DFT straintronic studies of single-layer [20–23] phosphorene exist which predict strongly exchange-correlation potential dependent results of limited predictability. They all suggest favorable potential for tuning of electronic structure properties. However, as shown below, all DFT models predict too small band gaps, some models, such as PBE [24] by as much as ≈ 2 eV, others, such as hybrid functionals HSE06 [25] or B3LYP [26], improve somewhat the band gap but result in less accurate equilibrium structures. Furthermore, the tuning area over which the band gap can be tuned without change of the direct nature of the $\Gamma \to \Gamma$ band gap is also determined with very limited accuracy, irrespective of the functional. Hence, the DFT models do *not* provide a reliable basis for determination of the stress tuning of electronic properties.

In order to consolidate the situation and fully rationalize the effect of strain on the band gap, we employ here a highly accurate many-body fixed-node QMC study of the key electronic quantities for the free-standing phosphorene under strain. In particular, benchmark-quality quasiparticle band gap has been determined for a wide range of applied strain and the boundaries between the different band-gap types determined: (i) between the direct ($\Gamma \to \Gamma$) and direct but reordered ($\Gamma \to \Gamma'$) excitations that also imply substantial differences of corresponding transport properties; and (ii) between the

direct $\Gamma \to \Gamma$ and indirect $\Gamma \to X$ excitations, see Fig. 4 for details. In our previous study of single-layer phosphorene in equilibrium [10] the unit cell parameters, a necessary prerequisite for any straintronic study, were only obtained from the experimental structure of 3D black phosphorus [27]. Here we obtained much better fundamentally anchored insights since all structural parameters have been relaxed in and out of equilibrium at the QMC level and therefore offer also improved equilibrium data [10]. In addition, the computed deformation potentials indicate out-of-plane auxetic behavior. For the purpose of methods benchmarking, our QMC results are compared with the ubiquitous DFT methods in commonly used approximations (GGA, hybrids) so as to offer insights into their biases.

II. METHODS

The electronic fundamental band gap is calculated as singlet-singlet vertical excitation energy

$$\Delta_f \approx E_v^{ss} = E_1^s - E_0^s, \tag{1}$$

with E_0/E_1 being the ground-/first-excited-states. We use periodic setups where E_0/E_1 were computed by the diffusion Monte Carlo (DMC) method in fixed-node approximation using variational Monte Carlo (VMC) trial wave functions with the nodal hypersurfaces determined by DFT orbitals using the generalized gradient approximation DFT-PBE [24], at the Γ point of the Brillouin zone, with short-range correlations described by the Jastrow factor [18]. DFT calculations, in addition to the DFT-PBE, have also been performed with PBE-HSE [25] and PBE-B3LYP [26] functionals.

The strain was applied in both armchair and zigzag direction by adjusting the a and b lattice parameters, see Fig. 1, considering deformations of up to $\approx \pm 10\%$. Determination of strained properties is treated as a full optimization problem in the space of four structural variables: lattice parameters a, b and two internal parameters x, y, see Fig. 1. Around the minima the data for E_0 were fitted by 4D paraboloid functions used to find the lowest point on the x, y subspace, leaving us to further minimize only bivariate functions $E_0 = f(a, b)$. The excited state E_1 is computed only at the minimum for the internal parameters x, y.

Finite-size scaling was performed for a series of periodic supercells, see Fig. 2, with $N/N_e = 11/220$, 16/320, 18/360, and 22/440 primitive unit cells/number of electrons for
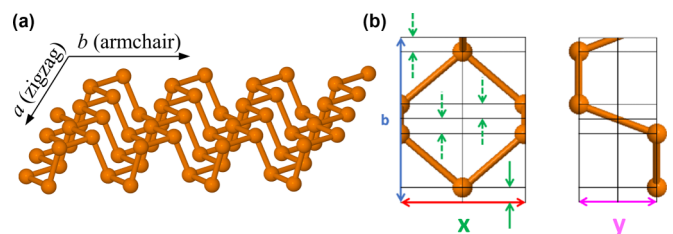

FIG. 1. Structure and basic structural parameters of single-layer phosphorene. (a) Structure of phosphorene with the two characteristic directions, *armchair* and *zigzag*, indicated. Note that the zigzag direction is along the a and armchair along the b lattice parameter. (b) Definition of the four basic structural parameters a, b, x, y.
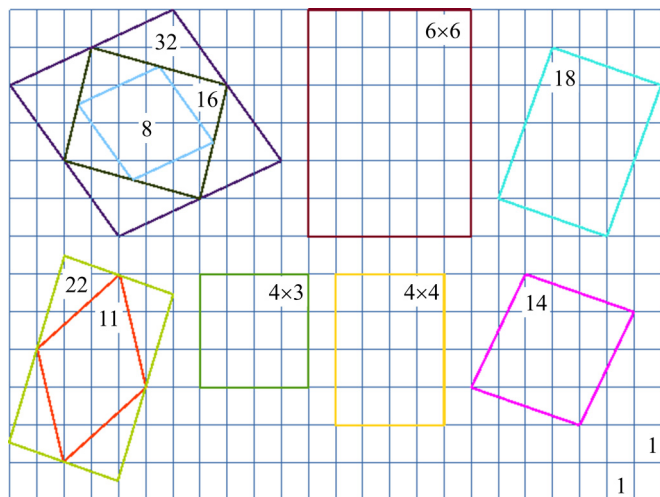
FIG. 2. Structural approximants. Various structural supercell sizes considered for selection of finite-size scaling: supercells containing 4×3, 4×4, 6×6, 8, 11, 14, 16, 18, 22, and 32 primitive unit cells. Note that all these supercells refold the Γ point but not all do refold the X point, for instance, 11 or 4×3.

$\Gamma \rightarrow \Gamma$ transitions and with 14/280, 16/320, 18/360, and 22/440 supercells for the $\Gamma \rightarrow$ K transition, using linear scaling with $1/N$ [10]. The convergence study in Table II in Appendix C shows that starting from the 11 structure, the energies per unit cell are converged within a few hundredths of an eV. The DFT convergence of lattice parameters exhibits similar trends. Figure 3 depicts the scaling behavior for the seven points bracketing the zero-strain state in the *ab* plane, see Fig. 1 and Fig. 4, used in the real calculation for constructing Fig. 5 ($\Gamma \rightarrow \Gamma$) and Fig. 7 ($\Gamma \rightarrow \Gamma'$ and $\Gamma \rightarrow$ X). The band gaps are believed to be statistically converged to within the chemical accuracy.
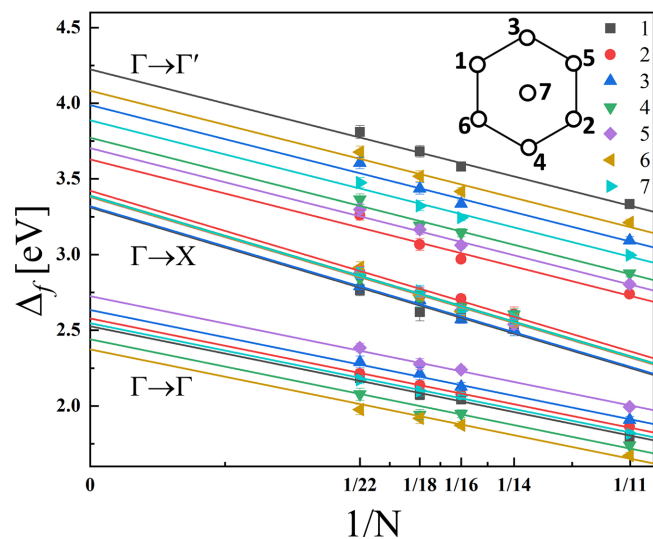

FIG. 3. Finite-size scaling for all seven points, see the inset, used in the paraboloid approximation for the $\Gamma \rightarrow \Gamma$, $\Gamma \rightarrow$ X, and $\Gamma \rightarrow \Gamma'$ transitions.
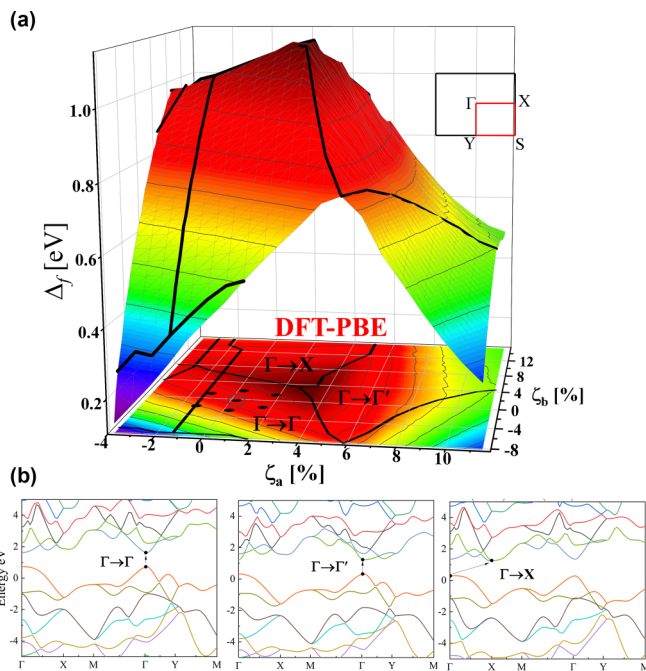

FIG. 4. The effect of strain. (a) The effect of strain on the nature of the band gap in single-layer phosphorene in the DFT-PBE description. The different black lines outline the different band gaps. The region corresponding to the direct $\Gamma \rightarrow \Gamma$ transition is indicated as well as the related $\Gamma \rightarrow \Gamma'$ transition with the LUMO/LUMO + 1 bands interchanged, and the $\Gamma \rightarrow$ X transition; for more details, see panel (b), the text, and Fig. 11 in Appendix E. The seven points are the primary points on which the fixed-node DMC calculations were performed; the circle indicating the point corresponding to unstrained structure. The inset depicts the 2D Brillouin zone of phosphorene. Positive/negative strain correspond to tensile/compressive strain. (b) Illustration of the different band gap types $\Gamma \rightarrow \Gamma$ (ζ_a=+0.32%, ζ_b=+0.11%), $\Gamma \rightarrow \Gamma'$ (ζ_a=+5.93%, ζ_b=+1.62%), and $\Gamma \rightarrow$ X (ζ_a=-2.09%, ζ_b=+8.49%) in the DFT-PBE description.

The strained gap surfaces were constructed as follows. For each supercell choice two paraboloids, one for the ground state (E_0) and one for the excited state (E_1) were constructed, see Fig. 9 in Appendix C. From four gap values (11, 16, 18, and 22 approximants for the $\Gamma \rightarrow \Gamma$ excitations and 14, 16, 18, and 22 approximants for the $\Gamma \rightarrow$ X excitations) the infinite-size limit was extracted. This gave seven explicitly QMC calculated values (1−7, see Fig. 3) through which a quadratic form was fitted for the $\Gamma \rightarrow \Gamma$, $\Gamma \rightarrow \Gamma'$, and $\Gamma \rightarrow$ X transitions:

$$\Delta_f(a, b) = c_0 + c_1 \times a + c_2 \times b + c_3 \times a^2 + c_4 \times b^2$$
$$+ c_5 \times a \times b. \tag{2}$$

The same Eq. (2) was also used to fit the deformation energies E_0. The results are compiled in Table I in Appendix B.

QMC calculations were mostly performed with the QMCPACK suite of codes [28]. Part of the QMC calculation was also done using the TurboRVB package [29]. All DFT calculations were done with the Quantum Espresso package [30].

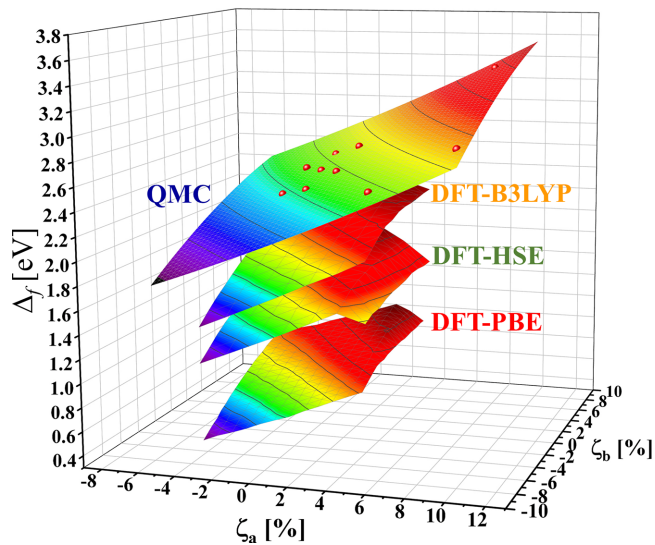Further technical details can be found online [31].

FIG. 5. Fundamental gap under strain. Fundamental gap Δ_f as calculated in fixed-node QMC and in DFT with various exchange-correlation (xc) functionals (PBE, HSE, B3LYP). The QMC data is represented by the red points with error bars corresponding to the symbol size.

III. RESULTS AND DISCUSSION

In order to set the stage, we first scan the band gap response to strain by DFT-PBE techniques. The results are shown in Fig. 4(a). In equilibrium, the band gap in phosphorene is direct at Γ [32]. As shown in detail in Appendix E, application of strain in general modifies the nature of the band gap and a number of gap types corresponding to different transitions occur. However, as Figs. 4 and 11 indicate, the region where application of strain does *not* change the nature of the
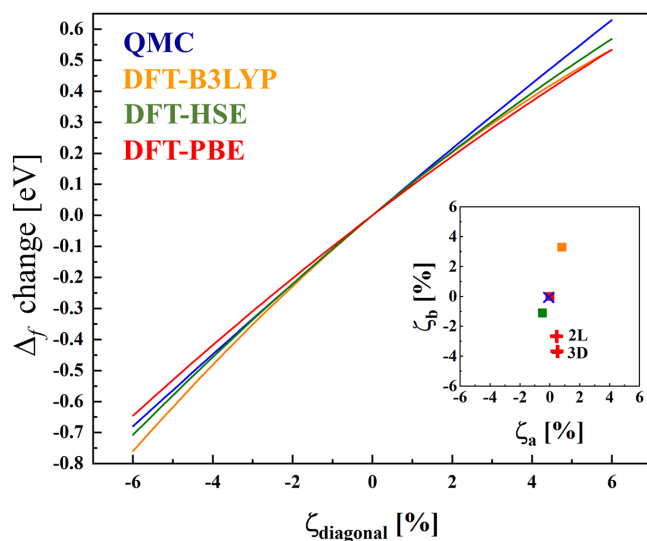

FIG. 6. Gauge factor. Change of Δ_f from applied diagonal strain with respect to the equilibrium Δ_f within each approach. The inset shows the locations of corresponding minima including the minima for a bilayer (2L) and black phosphorus crystal (3D) obtained by using the PBE + D3 functional [33]. Zero corresponds to the fixed-node QMC result shown by blue cross.

excitation (direct at Γ) is remarkably large in SLP. Accordingly, we have selected our QMC calculations to be confined primarily to that region. In principle, the QMC boundaries of the direct $\Gamma \to \Gamma$ transition could all be determined. We have localized two such boundaries: (i) the boundary between the $\Gamma \to \Gamma$ and $\Gamma \to \Gamma'$ where the order of LUMO (Lowest Unoccupied Molecular Orbital) and LUMO + 1 is exchanged, and (ii) the boundary between the $\Gamma \to \Gamma$ and $\Gamma \to X$ transition, see Figs. 4 and 7.

A. Band-gap response to strain and gauge factor

The corresponding QMC and DFT-PBE/HSE/B3LYP *fundamental/quasiparticle gaps* are shown in Fig. 5; parameters of the paraboloid fit are compiled in Table I in Appendix B. For DFT we consider $\zeta_a, \zeta_b \in \langle -4, +4 \rangle \%$ as a sufficiently large range for the $\Gamma \to \Gamma$ band gap. Our calculations below indicate that the $\Gamma \to \Gamma$ QMC band gap may cover a significantly wider interval, see Fig. 7 where we outline part of the boundaries. For our QMC optimized *structure at equilibrium* we obtain $a = 3.30 \pm 0.003$ Å, $b = 4.61 \pm 0.006$ Å, $x = 0.405 \pm 0.001$ Å, $y = 2.109 \pm 0.001$ Å, and $\Delta_f = 2.53 \pm 0.020$ eV. This value of the quasiparticle gap is in excellent agreement with the experimental value for freestanding SLP of 2.46 eV [34], keeping in mind that neglect of adiabatic, vibronic, and zero-point vibrational energy tends to increase the gap value compared to the experiments. The QMC optimized structure exhibits noticeable differences w.r.t. the structure derived from the 3D black phosphorus crystal [27] especially in the b parameter (a=3.324 Å and b=4.376 Å), see the inset in Fig. 5(b). All gaps in the DFT treatment are appreciably smaller than our QMC value. As expected, the smallest value by about 2 eV is obtained by the commonly used DFT-PBE functional. The hybrid functionals yield larger values but fail badly in predicting the equilibrium geometries, see the inset in Fig. 6, and also deformation energies as explained below.

The band-gap change due to applied biaxial strain is depicted in Fig. 6. This enables calculation of the *gauge factors*. Here QMC and DFT predict similar gauge factors of $\approx$110 meV/% strain. This rate is comparable to that experimentally determined for TMDs. For instance, in the quintessential straintronic material MoS_2, experimental values for the uniaxial gauge factors for A/B excitons vary in a wide range of $\approx (40 - 125)$ meV/% [35]. Experimentally, the biaxial gauge factors are found 2.3 times the uniaxial strain ones [36] which would correspond to experimental biaxial gauge factors of $\approx (92 - 288)$ meV/%, placing our calculated biaxial gauge factor for phosphorene into the window determined experimentally for MoS_2. The main difference between phosphorene and MoS_2 is in the region of tunability without affecting the direct nature of the band gap. This limits the applicable (tensile) strains to $\approx 0.5\%$ in MoS_2 [37]. By contrast, in SLP the QMC predicts the tunability range over many percent, equally both in armchair and zigzag direction, see below. The finding that the band-gap tuning is fairly isotropic in a very anisotropic material, as phosphorene [8], is surprising. Hence, compared to TMDs, phosphorene opens a huge, larger by an order of magnitude, window for band-gap strain tunability.
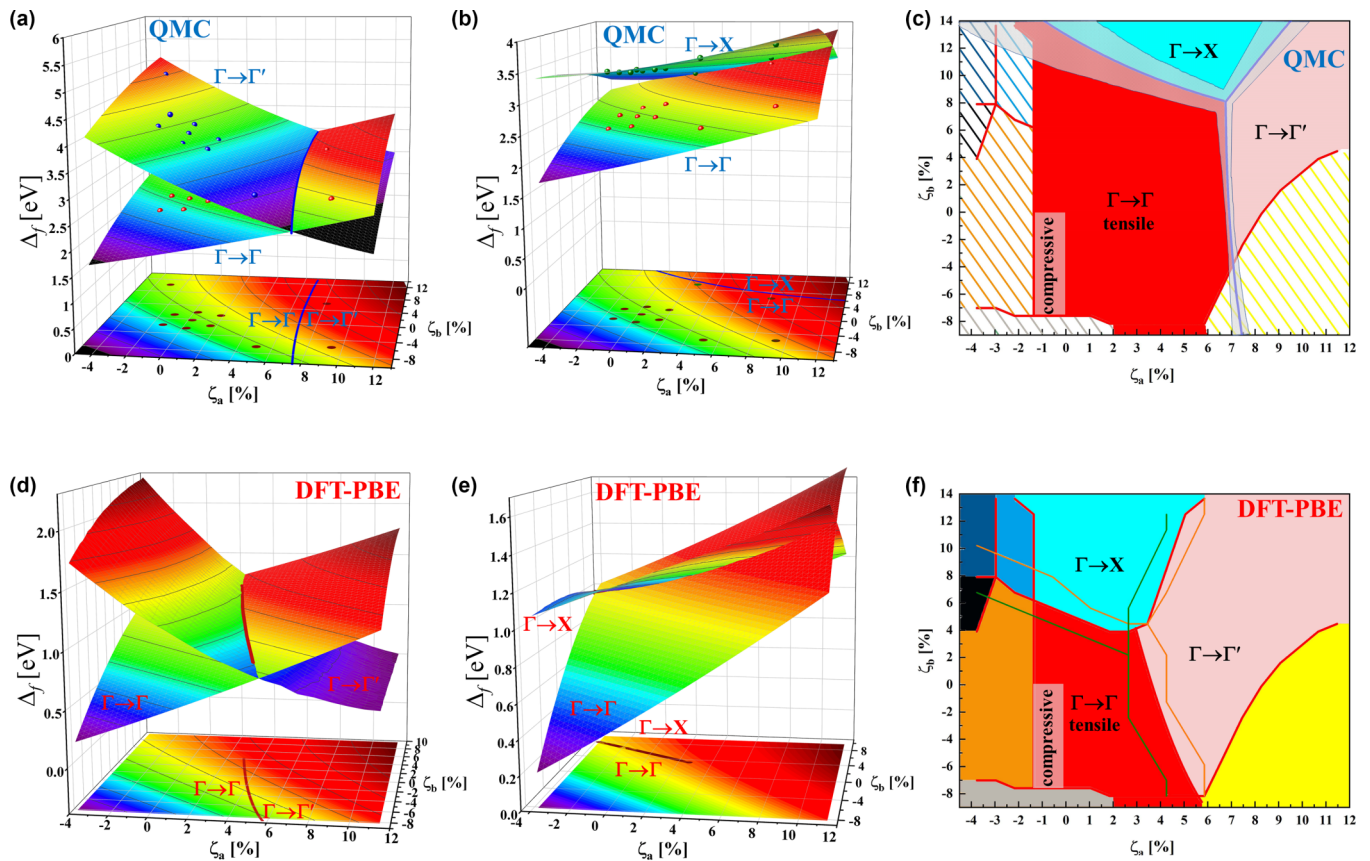
FIG. 7. Boundaries between $\Gamma \rightarrow \Gamma$, $\Gamma \rightarrow \Gamma'$, and $\Gamma \rightarrow X$. (a) The boundary between $\Gamma \rightarrow \Gamma$ and $\Gamma \rightarrow \Gamma'$, see the text, as calculated in fixed-node QMC. (b) The same but for the $\Gamma \rightarrow \Gamma$ and $\Gamma \rightarrow X$. (c) The boundaries between the different gap types as calculated in fixed-node QMC. Blue lines correspond to fixed-node QMC results with the overlays outlining the $\pm 1\sigma$ error bar, hatched regions correspond to DFT-PBE results. For color coding, see Fig. 11. Note that additional points have been included for the QMC Δ_f surfaces in order to cover a wider range of strains; for their precise location see Fig. 11 in Appendix E. The error bars are given by the symbol sizes. (d)−(f) The corresponding DFT-PBE results; the contour plots show, in addition to the DFT-PBE results (red line), also the DFT-HSE (green line) and DFT-B3LYP results (orange line).

B. Boundaries between different excitations

The different band gaps corresponding to different excitations are studied in the DFT-PBE model in Appendix E (Fig. 11). In order to demonstrate the much wider range of strains maintaining the $\Gamma \rightarrow \Gamma$ nature of the band gap, we have calculated the *boundary* between the $\Gamma \rightarrow \Gamma$ and a band gap at Γ formed by interchange of LUMO and LUMO + 1 states ($\Gamma \rightarrow \Gamma'$) and the boundary between the $\Gamma \rightarrow \Gamma$ and $\Gamma \rightarrow X$ due to applied strain, see Fig. 7 and Fig. 11 in
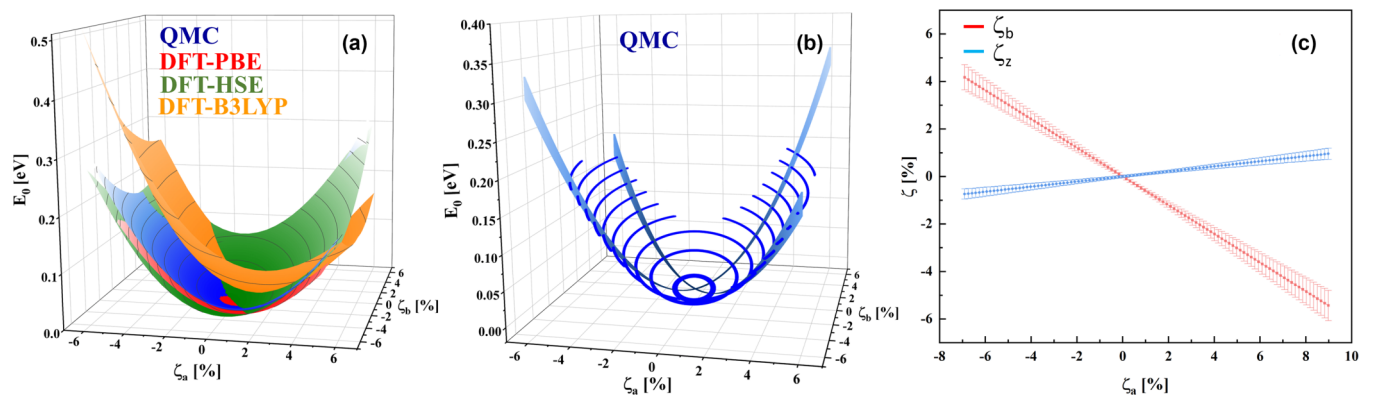

FIG. 8. Ground-state properties. (a) Deformation energies, in eV/unit cell, in fixed-node QMC and with DFT-PBE, HSE, and B3LYP functionals. Panel (b) shows the QMC result with the error bars superimposed. (c) Relations between in-plane (ζ_a, ζ_b) and out-of-plane (ζ_z) strains showing positive Poisson's ratio between in-plane strains and negative ratio between in-plane and out-of-plane strains.
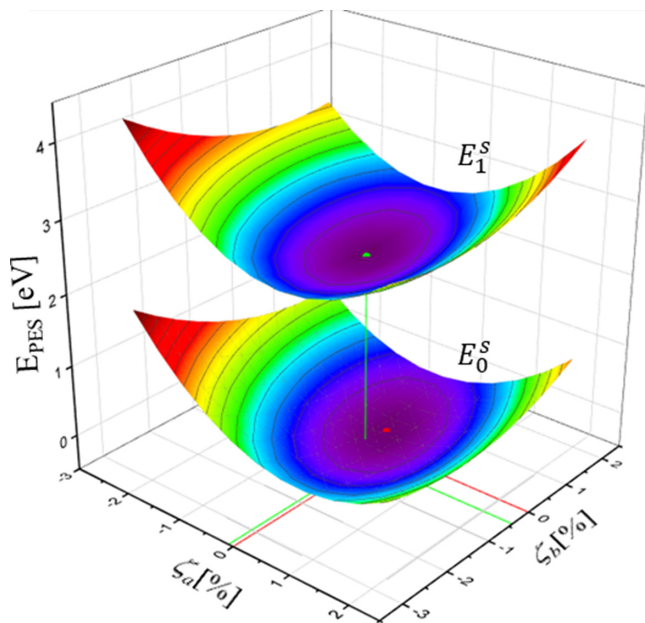
FIG. 9. Parabolloids corresponding of ground- and excited-state energies under strain. Example of the paraboloids (internal degrees of freedom at equilibrium) of the ground- (E_0^s) and excited-states (E_1^s) for a 4×4 approximant. The red/green lines indicate the offset of the ground- (green) and excited-state (red) paraboloids in the (ζ_a, ζ_b) plane.

Appendix E. The band gap strain tuning in those three areas ($\Gamma \to \Gamma$, $\Gamma \to \Gamma'$, $\Gamma \to X$) is determined as well. As for the first boundary, while both gaps are direct at Γ, the nature of the excited state is different if the order of unoccupied
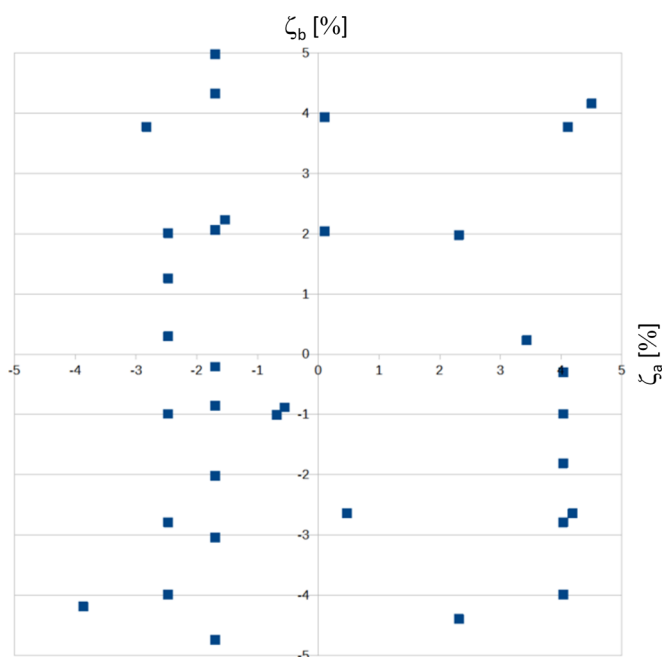

FIG. 10. Simulation of exfoliation of single-layer phosphorene onto quartz. Each point corresponds to a particular type of exfoliation dictated by the angle between the quartz and phosphorene lattices. The angle of the phosphorene lattice is kept rectangular.

states is interchanged ($\Gamma \to \Gamma'$). The new LUMO state has a differing curvature, hence, the transport properties in the conductance band are expected to be significantly modified. Figure 7 shows the boundary in the (ζ_a, ζ_b) plane calculated as an intersection between energies with the LUMO/LUMO+1 occupation. This boundary is seen to be shifted to significantly larger strains of $\approx +8\%$ in ζ_a, compared to $\approx +5\%$ in the DFT-PBE/HSE/B3LYP models. We note that the discovered huge area of the $\Gamma \to \Gamma'$ strain-induced excitations induces also change of transport properties through the excitation. A similar huge increase in the boundary between $\Gamma \to \Gamma$ and $\Gamma \to X$ is seen in the QMC description. Complete QMC and DFT maps are shown in panels (c) and (f), respectively. Hence, in reality, both boundaries are pushed rather close to the mechanical breakdown of the material. We note that the QMC-outlined boundaries outline a strain tuning area for the direct $\Gamma \to \Gamma$ band gap more than twice larger than that determined by DFT and that it extends mostly into the region of tensile strain, Fig. 7(c). We presume tensile strain to be more easily applied compared to the compressive strain which may induce wrinkling at higher compressive loads. Hence, the range of band-gap tuning by applied strain while maintaining the direct band gap at Γ is truly huge with achievable values of the band gap in the range 2.1–3.8 eV. In reality the tuning interval may be larger still as the boundaries to indirect gap regions corresponding to compressive strains have only been determined by DFT-PBE and we expect the boundaries to shift more further out to larger compressive strains and, hence, lower band gaps.

C. Deformation energies and negative Poison's ration

Finally, we discuss the *deformation energies* (QMC and DFT-PBE/HSE/B3LYP) which we have determined as byproducts of the calculated strained band gaps, Fig. 8; parameters of the paraboloid fits can be found in Appendix B. Deformation energy confirms the isotropic response of single-layer phosphorene to strain. The various DFT models lead to quantitative differences mainly caused by variations in equilibrium lattice parameters, see the inset in Fig. 6 and Ref. [31]. Since the equilibrium lattice parameters in the DFT-PBE are very accurately described by PBE and the curvature of E_0 is akin to that of fixed-node QMC, the deformation energy follows similar behavior. DFT-HSE exhibits similar curvature but the equilibrium geometry is slightly offset which translates to a less accurate description of the deformation energy. DFT-B3LYP has a very different equilibrium geometry, especially in the *b* parameter and much steeper curvature, and hence, represents the least accurate description of the deformation energy.

Negative *Poisson's ratio* was claimed to be present in single- [38] and few-layer [39] phosphorene. However, the cross-plane interlayer negative Poisson's ratio primarily probes the weak van der Waals interactions, while the property in single-layer phosphorene was obtained only via DFT-PBE modeling. Our fixed-node QMC data allow an accurate analysis of this property. In Fig. 8(c) the relation between in-plane (ζ_a, ζ_b) and out-of-plane (ζ_z) strains is shown. The in-plane strain relation clearly indicates a positive Poisson's ratio. At variance, the relation between in- and out-of-plane strains
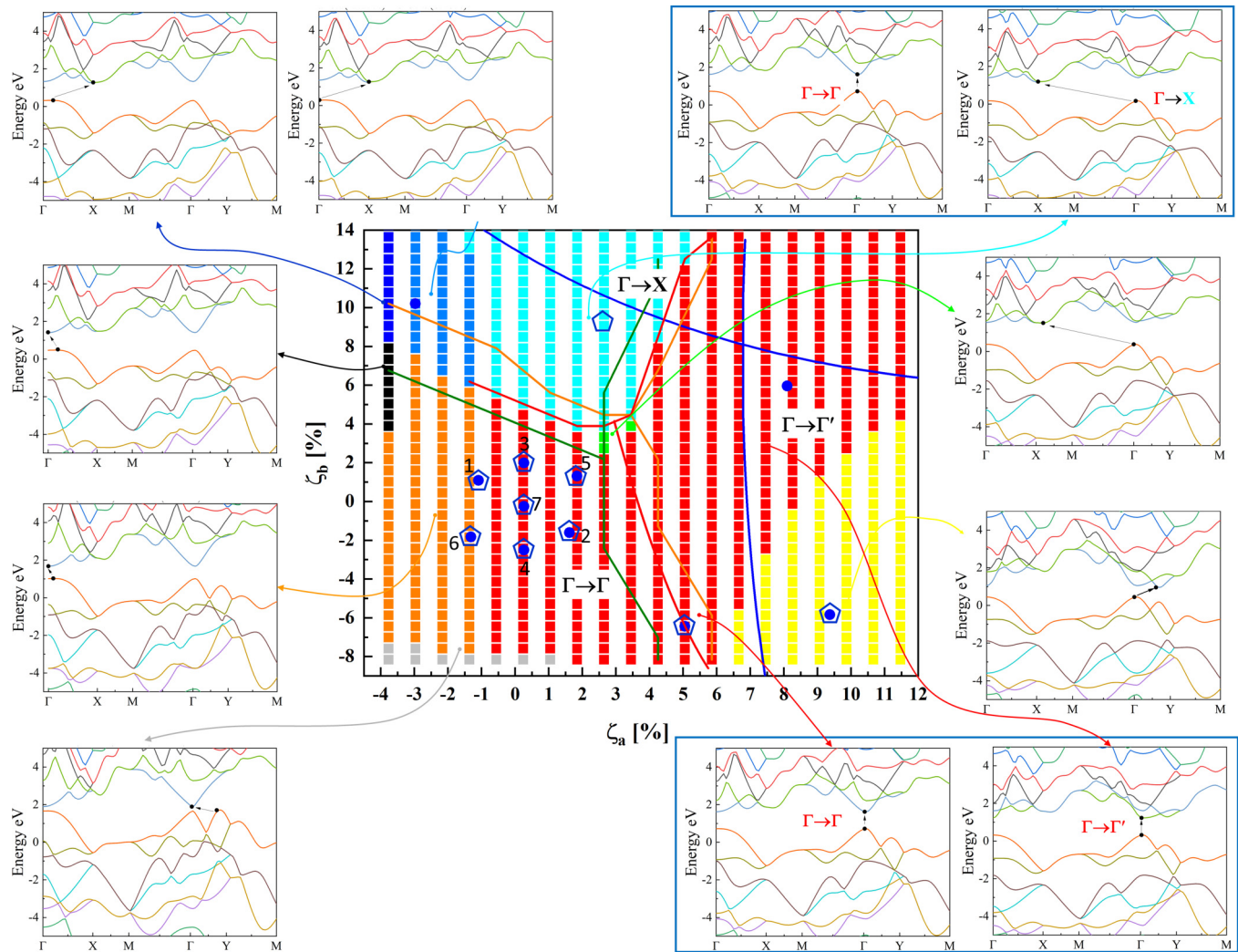
FIG. 11. The effect of strain on the nature of the band gap in single-layer phosphorene. The figure details the information in Fig. 4 of the main text, except that the nature of the band gap is demonstrated in detail by showing the representative PBE-calculated band structures with the excitation forming the band gap indicated. The areas depicted in red/light blue outline the $\Gamma \rightarrow \Gamma / \Gamma \rightarrow X$ transitions which are of primary interest here. The blue lines indicate the QMC-calculated boundaries outlining the change in the LUMO state forming the gap; the corresponding gap is labeled as $\Gamma \rightarrow \Gamma'$ and the $\Gamma \rightarrow X$ transitions, see also the band structures in the dark blue rectangles. The DFT-calculated boundaries in the PBE/HSE/B3LYP models are outlined by red/green/orange lines. For more details, see Fig. 7 of the main text. The blue dots/pentagons depict the points on which the fixed-node QMC calculations were performed for the $\Gamma \rightarrow \Gamma / \Gamma \rightarrow X$ transitions.

leads to a negative Poisson's ratio, for more details, see Ref. [31].

The strong band-gap response to strain may also explain the strong effect induced by the substrate on the band gap. The experimental scatter of the band gap in single-layer phosphorene is on the order of ≈ 1 eV [10]. The presence of the substrate combines two different contributions: dielectric embedding and strain. The effect induced by strain in a heterojunction, such as SLP/quartz or SLP/sapphire, is very hard to estimate as the formed moiré structures exhibit twist-angle dependence, and introduce inhomogeneous strain and an additional k-point dependence of the band gap. Disregarding these complexities and approximating the heterointerface by interlocked supercells, one can induce strains by several percent which could change the band gap in the range of ≈ 1 eV as also found in experiments, see Fig. 10 in Appendix D.

IV. SUMMARY AND CONCLUSIONS

In summary, using benchmark-quality diffusion Monte Carlo methods, we have calculated the effect of applied strain on quasiparticle band gap in phosphorene. Our study has revealed a huge tuning window, mostly in tensile region, for applied strain, about an order of magnitude larger than in MoS_2, regarded to be the model straintronic material. This huge tuning window is due to a combination of a high gauge factor and large window of applied strains leaving the direct $\Gamma \rightarrow \Gamma$ nature of band gap unchanged. The width of the tuning window is close to the mechanical breakage point of the material. In addition, we have also determined the equilibrium structure of the free-standing material, which is not known experimentally. Our calculated quasiparticle band gap in equilibrium is within chemical accuracy from the experimental

value for the free-standing phosphorene. The QMC results are compared with results of several DFT functionals providing insights into corresponding DFT inaccuracies and making an educated use of the much cheaper DFT calculations possible. We expect that the QMC methods, still rarely used to the growing family of 2D materials, to become the method of choice in future high accuracy studies of 2D materials.

ACKNOWLEDGMENTS

APPENDIX A: CHARACTER OF GROUND- AND EXCITED-STATE STRAINED ENERGY SURFACES

From Fig. 3 follows that the scaling curves corresponding to various strain for a given excitation are mutually parallel. This finding is highly nontrivial, considering the way they are calculated, Eq. (1). This finding can be rationalized by inspecting the ground- and excited-state paraboloids in Fig. 9. The linear scaling with the system size essentially means that the shape of the paraboloids has converged and the only parameter evolving is the vertical (energy) offset of the paraboloids. Furthermore, the gaps are not constant, meaning that there is also a "horizontal" offset of the paraboloids in the (ζ_a, ζ_b) plane, see the red and green lines in Fig. 9.

APPENDIX B: FITTED PARAMETERS OF STRAINED GAP AND DEFORMATION ENERGIES

Equation (2) was used to fit the strained band gaps and deformation energies E_0. The results are compiled in Table I.

APPENDIX C: CONVERGENCE OF STRUCTURAL PARAMETERS WITH THE SUPERCELL SIZE

Various structural approximants were considered for finite-size scaling, see Fig. 2. The selection of approximants was

TABLE I. Parameters of strained gap and deformation energy. Fitted parameters of Eq. (2) for $\Gamma \rightarrow \Gamma$, $\Gamma \rightarrow \Gamma'$, and $\Gamma \rightarrow X$ transitions and for deformation energies in various DFT and fixed-node QMC treatments.

	Band gap					
Transition	c_0	c_1	c_2	c_3	c_4	c_5
$\Gamma \rightarrow \Gamma$ (QMC)	3.947	-17.177	5.040	39.583	17.995	-14.222
$\Gamma \rightarrow \Gamma'$ (QMC)	3.950	-16.063	3.998	38.781	-7.039	-1.553
$\Gamma \rightarrow X$ (QMC)	3.340		2.384	-2.441	20.798	-6.051
	Deformation energy					
QMC	0.000	0.127	0.375	46.817	28.157	12.402
DFT-PBE	0.000	0.000	0.000	47.072	11.012	17.126
DFT-HSE	0.004	0.246	0.319	53.277	12.694	16.788
DFT-B3LYP	0.018	-1.637	-1.166	55.878	17.282	17.688

based on a DFT study of convergence of ground-state energy and structural parameters [31]. While the 4×3 and 4×4 approximants do not represent suitable supercells based on the ground-state energy convergence, starting from the 11 structure, the energies per unit cell are converged within a few hundredths of an eV. The DFT convergence of lattice parameters exhibits similar trends, see Table II.

APPENDIX D: THE EFFECT OF SUBSTRATE

Any 2D structure needs to be supported on a substrate in order to be able to conduct any experimental study on it. Phosphorene is typically exfoliated on SiO_2, sapphire, or h-BN. Specifically for phosphorene which is reactive, a capping layer is needed for longer term stability [32,40]. The support/capping layer modifies the dielectric embedding and possibly also subject the phosphorene to strain. The combination of these factors will modify the band gap from the value of the free-standing phosphorene studied here. We limit ourselves just to the effect of the strain induced by the substrate. Strain induced by substrate on a 2D material in a heterointerface is very complex due to formation of moiré structures. The moiré structure is twist-angle dependent, the strain induced is heterogeneous and the additional periodicity of the moiré structure introduces an additional k-point dependence of the band gap. Here we introduce much more a simplified picture by enclosing the interface into a supercell with edges much smaller than the moiré periodicity. In Fig. 10 we show a simulation of that effect by considering phosphorene exfoliation onto quartz. As can be seen, the points are scattered throughout the entire range of the strain window of $\pm 5\%$ considered here. The equivalent band-gap tuning due to this strain is in the range of ≈ 1eV, which explains the huge scatter in the band gaps experimentally observed.

APPENDIX E: CHARACTER OF THE BAND GAP UNDER STRAIN: DFT RESULTS

Prior to performing the costly fixed-node QMC calculations we have prescreened the response of single-layer phosphorene to strain at a DFT level. This study is based on the DFT-PBE xc functional which gives the equilibrium

TABLE II. Convergence of structural parameters. Evolution of structural parameters of the equilibrium structures (a, b, x, y, see Fig. 1 of the main text) and of energies of the ground- and excited-state (E_0^s, E_1^s) with the size of the approximant. Structural parameters are in a.u., energies are in eV/primitive unit cell. 3D-BP stands for the experimental structural parameters of 3D black phosphorus [27].

	QMC 11-cell	QMC 16-cell	QMC 22-cell	DFT-PBE	3D-BP
			Ground state		
a	$6.229 \pm 0.008\$	$6.238 \pm 0.002\$	$6.230 \pm 0.002\$	6.235	6.2618
b	$8.651 \pm 0.017\$	$8.688 \pm 0.008\$	$8.707 \pm 0.006\$	8.711	8.2700
x	$0.748 \pm 0.005\$	$0.759 \pm 0.002\$	$0.765 \pm 0.001\$	0.770	0.6367
y	$3.987 \pm 0.007\$	$3.978 \pm 0.003\$	$3.985 \pm 0.002\$	3.975	4.0280
E_0^s	$-716.563 \pm 0.002\$	$-716.498 \pm 0.0008\$	$-716.469 \pm 0.0007\$	-717.711	NA
			Excited state		
a	$6.227 \pm 0.027\$	$6.222 \pm 0.003\$	$6.224 \pm 0.003\$	6.222	NA
b	$8.515 \pm 0.178\$	$8.607 \pm 0.012\$	$8.664 \pm 0.010\$	8.543	NA
x	$0.728 \pm 0.044\$	$0.747 \pm 0.003\$	$0.761 \pm 0.002\$	0.739	NA
y	$4.053 \pm 0.018\$	$4.031 \pm 0.002\$	$4.020 \pm 0.002\$	4.051	NA
E_1^s	$-716.415 \pm 0.005\$	$-716.375 \pm 0.0007\$	$-716.375 \pm 0.001\$	-717.643	NA

geometry in very good agreement with our QMC modeling. The results are shown in Fig. 11 which outlines the various types of band gap which arise due to applied strain. Our conclusions at the DFT level are similar to those reached in the other DFT studies [20–23]. Only in the region in red is the gap strictly direct $\Gamma \rightarrow \Gamma$. Note that the $\Gamma \rightarrow \Gamma$ region (in red) borders with the $\Gamma \rightarrow X$ (in light blue) and a region where the DFT top of the valence band displaces slightly from the Γ point towards the X point, making the band gap indirect (in orange). Unlike the $\Gamma \rightarrow X$ which, similarly to $\Gamma \rightarrow \Gamma'$, is fairly easy to determine by fixed-node QMC techniques, the latter (orange) boundary is much tougher as it would require use of approximants with exorbitant sizes.

In summary, we have explicitly outlined using the fixed-node QMC techniques on the boundaries between the $\Gamma \rightarrow \Gamma$ and $\Gamma \rightarrow \Gamma'$ band gaps which arise due the change of the order of the LUMO and LUMO + 1 states under pressure and the $\Gamma \rightarrow \Gamma$ and $\Gamma \rightarrow X$, see the illustrative band structures in the blue boxes of Fig. 11. Note that the two bands involved in the $\Gamma \rightarrow \Gamma'$ transition are significantly different as will be the electronic/transport properties in those two states. Due to inherent numerical limitations, no attempt was made to determine the other boundaries. Note also that the DFT- and QMC-calculated boundaries are significantly different and that the QMC boundaries are shifted to significantly larger strains, see also Figs. 4, 7, and the accompanying discussion in the main text.

[1] L. Li, Y. Yu, G. J. Ye, Q. Ge., X. Ou., H. Wu, D. Feng, X. H. Chen., and Y. Zhang, Black phosphorus field-effect transistors, Nat. Nanotechnol. **9**, 372 (2014).

[2] H. Liu, A. T. Neal, Z. Zhou, Z. Luo, X. Xu, D. Tomanek, and P. D. Ye, Phosphorene: An Unexplored 2D Semiconductor with a High Hole Mobility, ACS Nano **8**, 4033 (2014).

[3] K. Novoselov, A. Geim, S. Morozov, D. Jiang, Y. Zhang, S. Dubonos, I. Grigorieva, and A. Firsov, Electric Field Effect in Atomically Thin Carbon Films, Science **306**, 666 (2004).

[4] B. Hunt, J. D. Sanchez-Yamagishi, A. F. Young, M. Yankowitz, B. J. LeRoy, K. Watanabe, T. Taniguchi, P. Moon, M. Koshino, P. Jarillo-Herrero, and R. Ashoori, Massive Dirac Fermions and Hofstadter Butterfly in a van der Waals Heterostructure, Science **340**, 1427 (2013).

[5] K. F. Mak, C. Lee, J. Hone, J. Shan, and T. F. Heinz, Atomically Thin MoS₂: A New Direct-Gap Semiconductor, Phys. Rev. Lett. **105**, 136805 (2010).

[6] K. Watanabe, T. Taniguchi, and K. Hisao, Direct-bandgap properties and evidence for ultraviolet lasing of hexagonal boron nitride single crystal, Nat. Mater. **3**, 404 (2004).

[7] W. Han, R. Kawakami, M. Gmitra, and J. Fabian, Graphene spintronics, Nat. Nanotechnol. **9**, 794 (2014).

[8] A. Castellanos-Gomez, Black Phosphorus: Narrow Gap, Wide Applications, J. Phys. Chem. Lett. **6**, 4280 (2015).

[9] R. Ganatra and Q. Zhang, Few-Layer MoS₂: A Promising Layered Semiconductor, ACS Nano **8**, 4074 (2014).

[10] T. Frank, R. Derian, K. Tokar, L. Mitas, J. Fabian, and I. Stich, Many-Body Quantum Monte Carlo Study of 2D Materials: Cohesion and Band Gap in Single-Layer Phosphorene, Phys. Rev. X **9**, 011018 (2019).

[11] F. Xia, H. Wang., and Y. Jia, Rediscovering black phosphorus as an anisotropic layered material for optoelectronics and electronics, Nat. Commun. **5**, 4458 (2014).

[12] J. Ryou, Y.-S. Kim, K. C. Santosh, and K. Cho, Monolayer MoS₂ bandgap modulation by dielectric environments and tunable bandgap transistors, Sci. Rep. **6**, 29184 (2016).

[13] R. Roldán, A. Castellanos-Gomez, E. Capelluti, and F. Guinea, F. Guinea, Strain engineering in semiconducting two-dimensional crystals, J. Phys.: Condens. Matter **27**, 313201 (2015).

[14] Z. Dai, L. Liu, and Z. Zhang, Strain Engineering of 2D Materials: Issues and Opportunities at the Interface, Adv. Mater. **31**, 1805417 (2019).

[15] S. Bertolazzi, J. Brivio, and A. Kis, Stretching and Breaking of Ultrathin MoS$_2$, ACS Nano **5**, 9703 (2011).

[16] Q. Wei and X. Peng, Superior mechanical flexibility of phosphorene and few-layer black phosphorus, Appl. Phys. Lett. **104**, 251915 (2014).

[17] K. He, C. Poole, K. Mak, and J. Shan, Experimental Demonstration of Continuous Electronic Structure Tuning via Strain in Atomically Thin MoS$_2$, Nano Lett. **13**, 2931 (2013).

[18] W. M. C. Foulkes, L. Mitas, R. J. Needs, and G. Rajagopal, Quantum Monte Carlo simulations of solids, Rev. Mod. Phys. **73**, 33 (2001).

[19] D. Wines, K. Saritas, and C. Ataca, A first-principles Quantum Monte Carlo study of two-dimensional (2D) GaSe, J. Chem. Phys. **153**, 154704 (2020).

[20] B. Sa, Y.-L. Li, J. Qi, R. Ahuja, and Z. Sun, Strain Engineering for Phosphorene: The Potential Application as a Photocatalyst, J. Phys. Chem. C **118**, 26560 (2014).

[21] X. Peng, Q. Wei, and A. Copple, Strain-engineered direct-indirect band gap transition and its mechanism in two-dimensional phosphorene, Phys. Rev. B **90**, 085402 (2014).

[22] Z. Zhang, Y. Zhao, and G. Ouyang, Strain Modulation of Electronic Properties of Monolayer Black Phosphorus, J. Phys. Chem. C **121**, 19296 (2017).

[23] H. V. Phuc, N. N. Hieu, V. V. Ilyasov, L. T. T. Phuong, and C. V. Nguyen, "First principles study of the electronic properties and band gap modulation of two-dimensional phosphorene monolayer: Effect of strain engineering," Superlattices and Microstructures, Superlattices Microstruct. **118**, 289 (2018).

[24] J. P. Perdew, K. Burke, and M. Ernzerhof, Generalized Gradient Approximation Made Simple, Phys. Rev. Lett. **77**, 3865 (1996).

[25] A. V. Krukau, O. A. Vydrov, A. F. Izmaylov, and G. E. Scuseria, Influence of the exchange screening parameter on the performance of screened hybrid functionals, J. Chem. Phys. **125**, 224106 (2006).

[26] P. J. Stephens, F. J. Delvin, C. F. Chabalowski, and M. J. Frisch, Ab initio calculation of vibrational absorption and circular dichroism spectra using density functional force fields, J. Phys. Chem. **98**, 11623 (1994).

[27] A. Brown and S. Rundqvist, Refinement of the crystal structure of black phosphorus, Acta Cryst. **19**, 684 (1965).

[28] J. Kim III *et al.*, QMCPACK: An open source *ab initio* quantum Monte Carlo package for the electronic structure of atoms, molecules and solids, J. Phys.: Condens. Matter **30**, 195901 (2018).

[29] K. Nakano *et al.*, TurboRVB: A many-body toolkit for *ab initio* electronic simulations by quantum Monte Carlo, J. Chem. Phys. **152**, 204121 (2020).

[30] P. Giannozzi *et al.*, QUANTUM ESPRESSO: A modular and open-source software project for quantum simulations of materials, J. Phys.: Condens. Matter **21**, 395502 (2009).

[31] More info on https://www.ui.sav.sk/w/wp-content/uploads/clanky/phospho_gap_strained_SM.pdf (2023).

[32] L. Li, J. Kim, C. Jin, G. J. Ye, D. Y. Qiu, F. H. da Jornada, Z. Shi, L. Chen, Z. Zhang, F. Yang, K. Watanabe, T. Taniguchi, W. Ren, S. G. Louie, X. H. Chen, Y. Zhang, and F. Wang, Direct observation of the layer-dependent electronic structure in phosphorene, Nat. Nanotechnol. **12**, 21 (2017).

[33] S. Grimme, J. Antony, S. Ehrlich, and H. J. Krieg, A consistent and accurate *ab initio* parametrization of density functional dispersion correction (DFT-D) for the 94 elements H-Pu, J. Chem. Phys. **132**, 154104 (2010).

[34] E. Gaufrès, F. Fossard, V. Gosselin, L. Sponza, F. Ducastelle, Z. Li, S. G. Louie, R. Martel, M. Côté, and A. Loiseau, Momentum-Resolved Dielectric Response of Free-Standing Mono-, Bi-, and Trilayer Black Phosphorus, Nano Lett. **19**, 8303 (2019).

[35] F. Carrascoso, H. Li, R. Frisenda, and A. Castellanos-Gomez, Strain engineering in single-, bi- and tri-layer MoS$_2$, MoSe$_2$, WS$_2$ and WSe$_2$, Nano Res. **14**, 1698 (2021).

[36] F. Carrascoso, R. Frisenda, and A. Castellanos-Gomez, Biaxial versus uniaxial strain tuning of single-layer MoS$_2$, Nano Mater. Sci. **4**, 44 (2022).

[37] Y. Huang, M. Manzoor, J. Brndiar, M. Milivojecic, and I. Stich, Straintronics with single-layer MoS$_2$: A quantum Monte Carlo study, In preparation (2023).

[38] J. W. Jiang and H. S. Park, Negative Poisson's ratio in single-layer black phosphorus, Nat. Commun. **5**, 4727 (2014).

[39] Y. Du, J. Maassen, W. Wu, Z. Luo, X. Xu, and P. D. Ye, Auxetic Black Phosphorus: A 2D Material with Negative Poisson's Ratio, Nano Lett. **16**, 6701 (2016).

[40] X. Wang, A. Jones, K. Seyler, V. Tran, Y. Jia, H. Zhao, H. Wang, L. Yang, X. Xu, and F. Xia, Highly anisotropic and robust excitons in monolayer black phosphorus, Nat. Nanotechnol. **10**, 517 (2015).